Atomic Spectroscopy

Article

Raman-based Characterization of Chang’e-6 Farside Lunar Soil: Insights into Non-mare Ejecta Composition and Lithological Diversity

Shuang Shi,[a] Xinyi Wang,[a] Kenan Cao,[a] Zhenbing She,[a,*] Zaicong Wang,[a,b,*] Qi He,[a] Tianyang Li,[a] Yiheng Li,[b] Jiaqi Zheng,[a] Xu Chen,[a] Long Xiao,[a,b] Biji Luo,[b] Keqing Zong,[a,b] Zhaochu Hu,[b] and Xiang Wu [a,b]

[a] Hubei Key Laboratory of Planetary Geology and Deep-Space Exploration, School of Earth Sciences, China University of Geosciences, Wuhan 430074, P. R. China

[b] State Key Laboratory of Geological Processes and Mineral Resources, School of Earth Sciences, China University of Geosciences, Wuhan 430074, P. R. China

Received: *August 08, 2025;* ***Revised:*** *September 14, 2025;* ***Accepted:*** *September 18, 2025;* ***Available online:*** *September 18, 2025.*

DOI: 10.46770/AS.2025.147

ABSTRACT: The Chang’e-6 (CE-6) mission returned the first farside lunar soil samples which are of great importance to understand the geological diversity and evolutionary history of the Moon. In this study, we employed a Raman-based automated particle analysis system to investigate the grain size and mineral composition of the CE-6 soil, which are compared with results of the nearside Chang’e-5 (CE-5) soil. Our analyses reveal that the CE-6 soil exhibit small grain size (mean = 4.4 μm) as the CE-5 soil, slightly exhibits higher plagioclase abundance (39.0 vs. 37.5 vol%), and lower pyroxene (18.4 vs. 39.4 vol%) and olivine (2.3 vs. 9.8 vol%) contents. Raman spectroscopic analysis further reveals a marked magnesium enrichment in CE-6 olivines (most grains with Fo of 40 − 90) compared to their CE-5 counterparts (most Fo < 60). Notably, evident compositional zonation in olivine (Fo of 66 to 47) is observed for a CE-6 lithic clast, which likely represents ejected crustal material with complex magmatic interactions. These findings support that the CE-6 scooped soil contains substantial non-mare components that is limited in the CE-5 sample. Given very low olivine abundance in the CE-6 landing site basalt, the wide range of olivine Fo in CE-6 soil reflects the contribution of olivine-bearing, mafic crustal lithologies such as magnesian-suite and ferroan anorthosite or even of material from the lunar mantle. This study highlights the capability of non-destructive, rapid and simultaneous determination of particle size and mineral composition with Raman-based analytical techniques, which enables direct analyses of complex soil samples and provides new insights into the mineral compositions of landing site basalts and also non-mare ejecta of the near and far sides of the Moon.

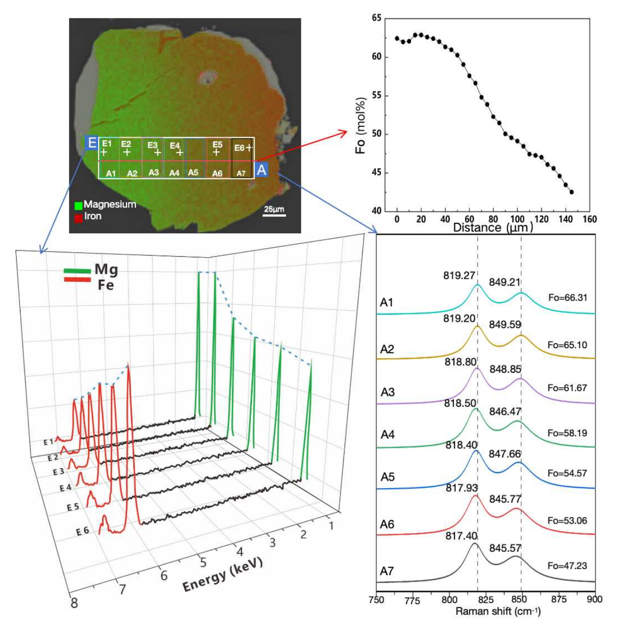

INTRODUCTION

In recent years, the study of lunar samples returned by the Chang’e-5 (CE-5) mission has significantly advanced our understanding of the Moon's geological history. The CE-5 samples have provided critical insights into the Moon's late-stage volcanic activity, mantle composition, and thermal evolution[1-4].On June 25, 2024, Chang’e-6 (CE-6) returned 1935.3 g of lunar soil samples from the Apollo basin of the South Pole-Aitken (SPA) Basin, one of the Moon’s oldest and most geologically complex regions, potentially containing materials from the lunar crust and upper mantle[5-8]. The different geological contexts of the CE-5 and CE-6 missions offer a new opportunity to address fundamental questions about the Moon's formation, differentiation, and evolution.

The application of advanced analytical techniques, including low-consumption, rapid compositional and grain-size analysis methods, has enabled high-resolution, multi-faceted characterization of the lunar samples, maximizing their scientific value[9,10]. The capability of Raman spectroscopy for mineral identification and characterization of planetary materials has been demonstrated[11-14]. Recently, the discovery of natural few-layer graphene in the CE-5 lunar soil using Raman spectroscopy has attracted much attention.[15] By using a Raman point-counting technique[16], additional information on mineral proportions and rock textures can be obtained. A new method has been developed to simultaneously measure the particle size and mineral constituents of CE-5 lunar soil.[10] Building on this study, we determined the particle size and modal abundances of the CE-6 soil with direct comparisons with results of the CE-5 soil. Furthermore, we extracted compositional data of pyroxene and olivine in the CE-6 and CE-5 soils from their Raman spectral features. Our results reveal notable differences in mineral composition, particle size distribution, and mineral chemistries between the CE-6 and CE-5 soils that are probably related to different magmatic processes of the lunar nearside and farside.

MATERIAL AND METHODOLOGY

Sample preparation. Lithic fragments with grain sizes > 50 µm were handpicked from the CE-6 soil sample (CE6C0200YJFM003, 500 mg), and were subsequently mounted in epoxy resin and carefully polished for detailed petrological and chemical analyses.

For automated particle analysis, small aliquots (ca. 30 µg each) of the CE-6 soil sample were taken from the subsample bottles and placed on 75 mm × 25 mm glass slides and then manually dispersed using tweezers. Prior to sample preparation, the tools were repeatedly cleaned with acetone, methanol and then ultra-pure water. After cleaning, the glass slides were checked in the dark field reflected light mode of the microscope to make sure there were no observable impurities on the surface. No organic solvent was used during the dispersion to minimize potential organic contamination.

Automated lunar soil particle analysis. Dispersed lunar soils were analyzed at the State Key Laboratory of Biogeology and Environmental Geology (BGEG), China University of Geosciences (Wuhan), utilizing a WITec α300R confocal Raman system integrated with the ParticleScout automated analysis platform (v5.3.14.106). High-resolution particle imaging was achieved through large-area stitching and focus-stacking techniques using dark-field objectives (20 ×, N.A. = 0.50; 50 ×, N.A. = 0.80). Particle detection employed brightness threshold segmentation, enabling quantitative reconstruction of spatial distribution maps.

For particle size analysis, measurements were conducted using optical microscopy imaging (dark-field objectives) integrated with the ParticleScout system. To minimize particle aggregation and stacking during sample preparation, particles with a solidity less than 0.85 (Table S1) were excluded. Size calibration followed a standardized protocol[10], incorporating three NIST-traceable particle standards (Duke Standards, Thermo Scientific) and two in-house references. Calibration equations were derived from linear regression of the five-standard dataset to correct raw particle size measurements. Calibrated particle size distributions are statistically summarized in Table S2.

For Raman-based mineral identification, lunar soil particles with grain size between 1 µm and 10 µm were selected. Automatic focusing was applied under the 50 × (N.A. = 0.80) dark field objectives during the analysis of each particle to obtain a spectrum with the highest signal to noise ratio. A 532 nm laser was used with an output laser power between 2.5 - 5 mW (Table S1). The integration time was set between 5 s and 6 s with 4 to 8 accumulations to obtain spectra with a fair quality (Table S1).

The documented phases include pyroxene, plagioclase, olivine, Fe-Ti oxides, glass and other minor or trace phases (*e.g.*, phosphate and quartz). Model abundances of these phases were calculated based on the sum of their spherical equivalent volume ($V_{SE} = \pi \times (d_{CE}^3/6)$), where d_{CE} refers to the circular equivalent diameter of the particles.

Raman point analysis and imaging. Raman point analysis were conducted on randomly selected pyroxene and olivine in polished grain mounts, using the same WITec α300R confocal Raman system. Laser excitation at 532 nm with output power at ca. 10 mW was used. Spectra were obtained using a 100 × (N.A. = 0.9) magnification objective with a 50 µm diameter optic fiber. A grating of 600 g/mm was used to achieve a wavenumber range of 4000 cm^{-1} and a spectral resolution of 4 cm^{-1}. Integration time for each spectrum varied from 10 to 20 s, and the number of accumulations from 10 to 15. The Raman spectra were collected at confocal depths of at least 0.5 µm below the thin section surface to minimize contamination. Large area Raman imaging was also performed on an olivine crystal to reveal compositional variations. A 532 nm laser was used with a power of 8 mW and focused with a 50 × (N.A. = 0.75) objective for 140 µm × 30 µm area scans. The targets for Raman imaging were examined under the reflected light to exclude areas of open cavities and popped-out grains that could have captured contaminants from polishing. The scans were controlled by a piezo-driven scanning stage, with a typical integration time between 0.3 s to 1 s per pixel. The WITec Project Five 5.1 Plus software was used to process the Raman spectra and

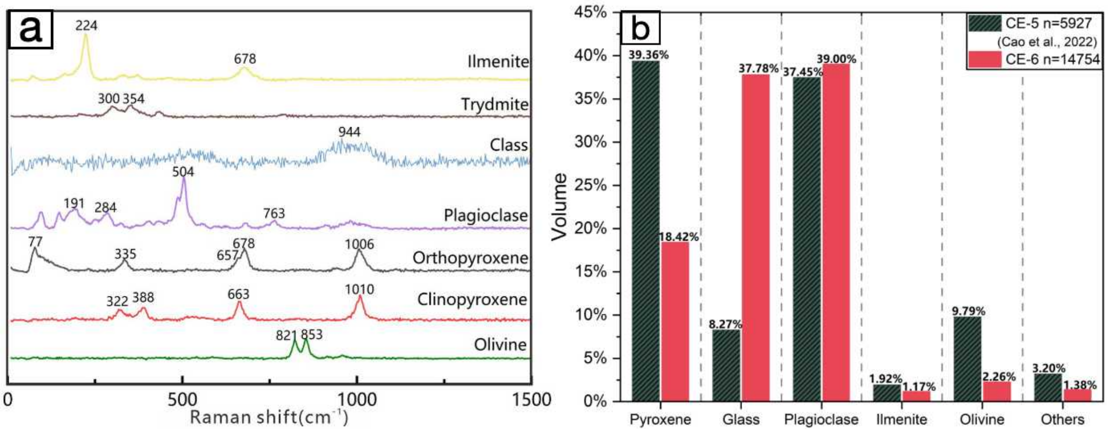

Fig. 1 Representative Raman spectra of main phases in CE-6 sample (a) and their volume percentages compared with CE-5 (b).

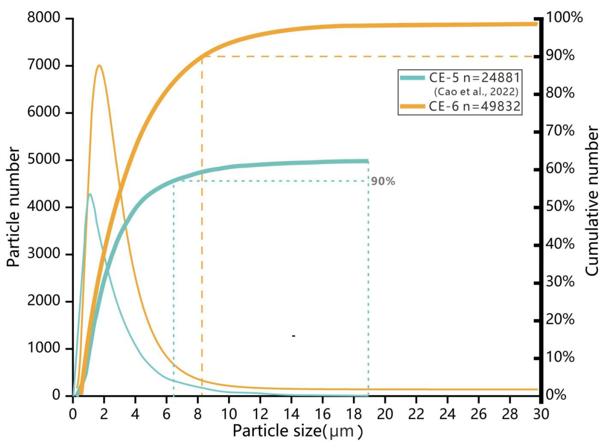

Fig. 2 Particle size distribution showing particle number and cumulative number of the CE-5 and CE-6 soils.

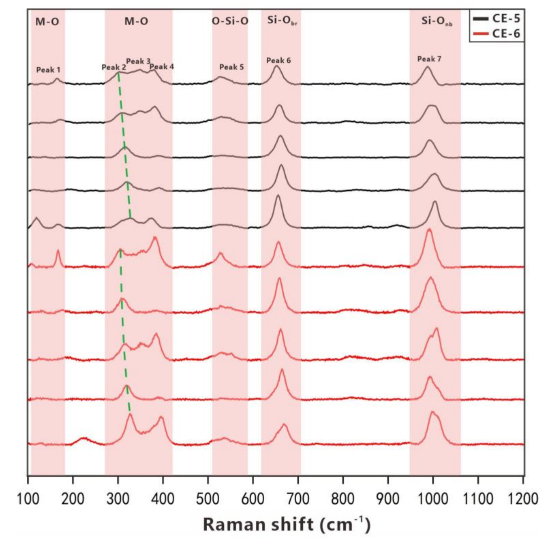

Fig. 3 Representative Raman spectra of pyroxenes in CE-5 and CE-6 samples and calculated w(MgO) and w(FeO) values. Peaks 1-4, SiO_4 rotation and metal-oxygen translation modes; Peak 5, O-Si-O bending bends; Peak 6, Si-O stretching mode of the bridging O atoms (Si-O_{br}); Peak 7, Si-O stretching vibrations related to the non-bridging Si-O bonds (Si-O_{nb}).

generate Raman images. Cosmic rays were removed under 2 cm^{-1} filter with a dynamic factor of 8. For the obtained Raman spectra, background was subtracted using the polynomial function (up to the 7th order) or the shape method.

Scanning electron microscopy and electron dispersive spectroscopy. Scanning electron microscopy (SEM) and electron dispersive spectroscopy (EDS) were conducted at BGEG with a Tescan VEGA 3 SEM equipped with an Oxford Instrument AztecOne XT EDS detector. Analyses of a polished grain mount were performed under a vacuum pressure of 10^{-3} mbar at 15 kV accelerating voltage, with working distances between 10 mm and 15 mm. The samples were coated with a nanometer layer of Au prior to analysis.

Electron probe microanalysis. Major elemental compositions of different minerals were determined using a JEOL JXA-8230 electron probe microanalyzer (EPMA) at the State Key Laboratory of Geological Processes and Mineral Resources, China University of Geosciences, Wuhan (GPMR- CUG). Minerals and impact melt glasses were analyzed using a 15-kV acceleration voltage and a 20 nA focused beam typically at 3 μm diameter for silicates. For silicate phases, the standards used for ZAF matrix correction were jadeite (Na), olivine (Si), diopside (Ca, Mg), almandine (Fe, Al), sanidine (K), rutile (Ti), rhodonite (Mn), and chromium oxide (Cr). The major elements of selected areas on the olivine crystal were obtained and the results are listed in Table S6.

RESULTS

Mineral constituents. The Raman-based particle analysis system enables simultaneous quantification of particle size distribution

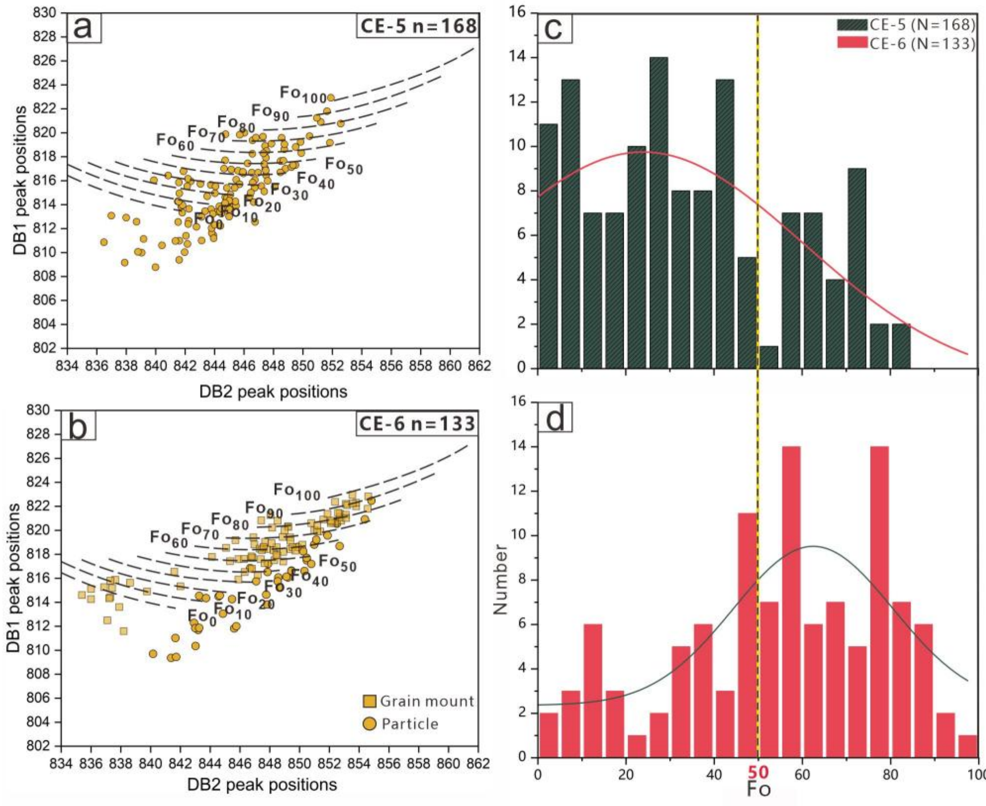

Fig. 4 Calculated Fo values for olivines from CE-5 and CE-6. (a-b) Scatter plot of olivine DB1 and DB2 peaks; (c-d) Histograms of Fo value. Reference line for Fo values from previous study[42].

and mineralogical constituents. CE-6 soil samples were subjected to three dispersions, from which six areas were selected for analysis (Fig S1, Table S1), collectively yielding the identification of 14,754 particles. Representative Raman spectra for the recognized phases in the CE-6 soil are shown in Fig. 1a.

The three subsamples of this study exhibit evident variations in terms of the abundances of glass (36.4 to 46.8 vol%) and pyroxene (13.4 to 18.9 vol%) (Table S3), indicating that the small sample size (ca. 30 μg per analysis) might have induced some uncertainties. Therefore, we consider that the summed results of the three subsamples more accurately represent the mineral constitution of the analysed CE-6 soil. The overall phase quantification reveals a mineral assemblage dominated by plagioclase (39.0 vol%, 36.5 wt%), glass (37.8 vol%, 35.4 wt%), and pyroxene (18.4% vol%, 21.7 wt%), with minor proportions of olivine (2.3% vol%, 3.2 wt%), Fe-oxides (1.2% vol%, 1.9 wt%), and accessory phases (1.4% vol%, 1.3% wt%) (Fig. 1b, Table S3).

Size distribution. Six analyses were performed on three dispersed samples from the CE-6 soil (Fig. S1), a total of 49, 832 particle size measurements were obtained, with size (circular equivalent diameters) ranging from 0.4 μm to 111.8 μm, the grain size analysis of several representative images is presented in Fig. S2. The central tendency parameters show a mean diameter of 4.4 μm, a median of 2.8 μm, and a mode of 1.6 μm (Table S2), while 90% of particles fall within the 0.4 – 8.2 μm range (Fig. 2). Minimum Feret diameters exhibit a slightly broader distribution (0.2 – 126.4 μm; mean = 3.9 μm), correlating with observed particle elongation as evidenced by the mean aspect ratio (AR = minor/major axis) of 0.77 (Table S2).

Chemistry of main silicate phases. Composition of pyroxene. For CE-5 samples, we randomly extracted Raman data for pyroxenes from ParticleScout and conducted Raman point analyses on pyroxenes in grain mounts, resulting in a total of 44 Raman spectra. For the CE-6 soil, random Raman point analysis of pyroxenes in grain mounts yielded 114 Raman spectra. MgO and FeO contents were calculated based on the position of the 303 − 330 cm^{-1} peak of pyroxene (Supplementary Note 1). The 44 Raman data points for CE-5 pyroxenes yielded average Mg and Fe weight percentages of w(MgO) = 9.9% and w(FeO) = 11.3%. In comparison, the CE-6 pyroxenes have slightly lower Mg (average w(MgO) = 9.3%) and higher Fe (average w(FeO) = 12.1%) contents (Fig. 3, Table S4). It is evident that the average FeO content in both CE-5 and CE-6 pyroxenes is higher than that of MgO, consistent with previous results[3, 6, 17].

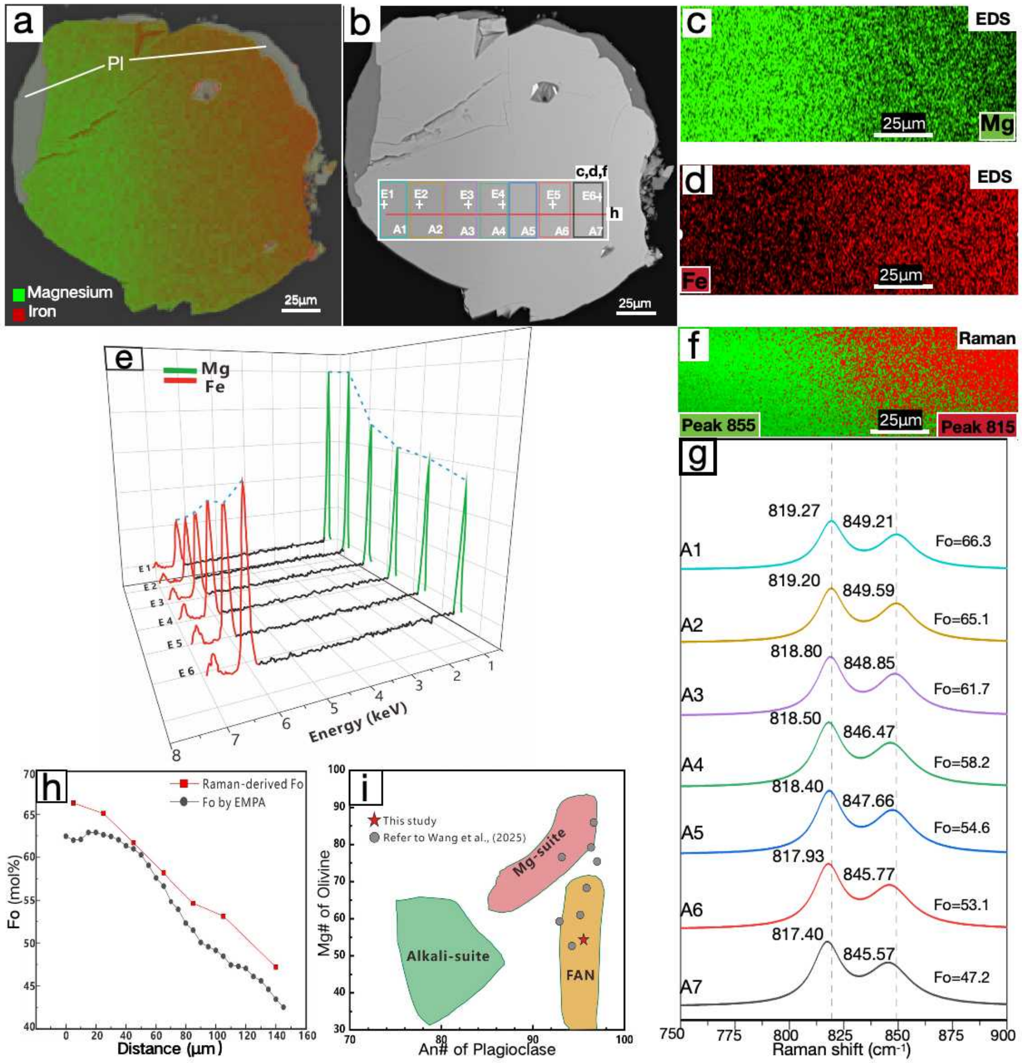

Fig. 5 Compositional variation of olivine in a lithic clast. (a) EDS map of Mg and Fe for the olivine overlain on BSE image; (b) Backscattered electron image of the clast; (c–d) EDS maps of the outlined area in (b) showing the distribution of Mg and Fe; (e) EDS spectra showing variations of Fe and Mg content for the spots (E1 to E7) marked in (b); (f) Raman map of the same area showing compositional variation in olivine; (g) Raman spectra of the 750 − 900 cm^{-1} region extracted from areas (A1 to A7) outlined in (b); (h) Fo profiles of the olivine determined by EMPA and Raman; (i) A plot of olivine Mg# of versus plagioclase An# in olivine-dominated lithic clast. The compositional fields for FAN, Mg-suite, and alkali-suite are based on established geological classifications[39].

It is also noted that Ca/(Mg + Fe + Ca) values (Wo content) may be extracted from the Raman features of quadrilateral pyroxenes[18], but it is more difficult because corrections based on structural information are needed for very low-Ca and very high-Ca samples. Interestingly, although pigeonite has similar Raman peaks at ∼660 cm^{-1} and ∼1000 cm^{-1} as orthopyroxene, it can be distinguished from the latter by the absence of a peak at ∼75 cm^{-1} that is always observed in the latter[19]. Further investigations of the Raman spectral features of various pyroxenes may lead to better methods for quantifying Ca/(Mg + Fe + Ca) values of pyroxenes, which are particularly important in aiding on-surface planetary exploration.

Fo values of olivine. From 14,754 particles in the CE-6 soil, we selected 45 olivines with strong Raman signals. Additionally, 88 olivine grains were selected from the grain mount for Raman point analysis, resulting in a total of 133 Raman spectra. For comparison, 168 olivine grains with strong Raman signals were selected from the 5,927 mineral particles in the CE-5 samples, to calculate Fo values using the DB1 peak (doublet peak #1, 815 − 825 cm^{-1}) and DB2 peak (doublet peak #2, 838 − 857 cm^{-1}) of olivine (Supplementary Note 2). The calculated olivine Fo values for CE-5 and CE-6 samples are presented in Fig. 4 and Table S5. The results indicate that in CE-5 samples, 80% of the olivines have Fo values lower than 50, which aligns closely with previous EPMA analysis[3]. Specifically, 42% of the CE-5 olivines have Fo <15, and 2% have Fo >75. In the CE-6 soil, ca. 52% of the olivines have Fo values greater than 50, 25% have Fo <15, and 23% have Fo >75 (Table S5). This is somewhat different from earlier EPMA analyses[6] (Table S8), which we think may be attributed to differences in analytical methods and sample representativeness.

Mineral chemistry of a lithic fragment. From the CE-6 grain mounts, we selected a lithic clast primarily consisting of olivine partly surrounded by plagioclase (Fig. 5a) for detailed analysis. EDS mapping revealed a zoned distribution of Fe and Mg in the olivine, with a complementary relationship between these two elements (Fig. 5a–d). EDS spot analyses confirmed the inverse relationship between the concentrations of Fe and Mg (Fig. 5e).

Raman hyperspectral images were created according to the intensities of the 815 cm^{-1} and 855 cm^{-1} peaks for olivine, which reflect the relative abundances of Fe and Mg in the olivine that are consistent with the EDS mapping (Fig. 5f). To improve the signal intensity of Raman spectra, we divided the Raman image data into seven sections (A1 to A7) to extract the summed Raman spectra for each section (Fig. 5g). The results showed progressive shifts of the DB1 and DB2 peaks to lower wavenumbers from A1 to A7, with the Fo value decreasing from 66.3 to 47.2 (Fig. 5g). This is confirmed by a transverse analysis in the same area by EPMA with a total of 30 data points, which yielded Fo values ranging from 62.4 to 42.5 (Fig. 5h; Table S6), closely matching the Raman-based estimations. In addition, EPMA analysis was conducted on feldspars surrounding the olivine (Fig. 5a–b), resulting in An# values ranging from 95.1 to 96.0 (Table S6, Fig. 5i).

DISCUSSION

Comparison of mineral constituents of CE-6 and CE-5 soils. Compared to results of the CE-5 sample determined with the same method[10], our analyses of the CE-6 samples show comparable plagioclase abundance (36.51 vs. 32.11 wt%) and substantial reductions in pyroxene (21.72 vs. 42.49 wt%) and olivine (3.21 vs. 9.79 wt%) proportions. The higher abundance of plagioclase in the CE-6 soil may account for its lower density compared with CE-5 soil (0.983 g/cm^3 vs. 1.2387g/cm^3, Li *et al.* [15]), as well as its higher Al_2O_3 and CaO and lower FeO content.[6,20] Collectively, these observations demonstrate a higher input of non-mare crustal ejecta for the CE-6 sample.[20]

The higher glass content in the CE-6 soil compared with CE-5 sample likely have resulted from the older age, and thus more intense space weathering of the CE-6 basalt[21, 22], as well as a significant contribution from ancient lunar crustal rocks that have experienced more impact. Input of volcanic glass is considered insignificant because this type of glass are extremely rare on the lunar surface (*e.g.*, only 3 volcanic glass out of ca. 3000 glass beads in the CE-5 soil[23]).

It is noteworthy that, compared to results of another aliquot of CE-6 scooped soil (CE6C0000YJFM00101) obtained by bulk soil XRD analysis (plagioclase 32.6 wt%, pyroxene 33.3 wt%, glass 29.4 wt%, olivine 0.5 wt%; Li *et al.* [15]), our data show higher glass and olivine contents, but significantly lower pyroxene abundance (Table S8). The slightly higher olivine abundances determined by Raman is attributable to the fact that olivines typically have stronger Raman signal than other phases in the lunar samples[10]. The much lower glass abundances determined by the XRD method[6] possibly represent an underestimated value because the lack of long-range order in amorphous materials would not result in well-defined peaks in the X-Ray spectra critical for accurate quantitative analysis[24]. The lower pyroxene content determined by Raman remains to be explained, but it is possibly a result of our analytical protocol that excludes unusually large particles (>10 μm) during the Raman-ParticleScout analysis.

Particle size features and sample heterogeneity of CE-6 lunar soils. When compared to CE-5 lunar soils analyzed using the same methodology[10], the CE-6 samples demonstrate coarser particle size characteristics, with increased mean (4.4 vs. 3.5 μm) and modal (1.6 vs. 1.0 μm) diameters. This difference in particle size can be attributed to ejecta from relatively young impact craters (*e.g.*, Chaffee S crater)[8, 25] that have not experienced prolonged space weathering. Moreover, these ejecta can quickly cover localized areas, forming a thicker layer of debris. A total of 26,785 craters with diameters greater than 50 meters were identified within the CE-6 landing zone[5]. Frequent impact events occur, leading to the deposition of new ejecta over older layers, which causes surface particles to retain their coarseness.[26]

Notably, while a bimodal size distribution was observed in another CE-6 aliquot (CE6C0000YJFM00101)[6]—a feature characteristic of immature Apollo lunar soils—this pattern was not shown in the current dataset. Our analyses of three subsamples yielded consistent results (Table S2), excluding significant sample heterogeneity for the CE-6 soil. As shown in Table S8, the sample size in our study is two orders of magnitude lower than that of previous study[6]. Thus, the discrepancy between our data and previous results may be attributed to different analytical methods and sample sizes and may be clarified by further analysis with larger sample amount.

Olivine Fo values as evidence of non-mare crustal ejecta. The remarkable compositional difference of olivines in the CE-5 and CE-6 soils (Fig. 4) likely reflect distinct geological history of the two landing sites. The CE-5 samples, returned from the lunar near side, are composed predominantly of local, highly evolved mare basalts with negligible contribution (<5%) from highland and KREEP materials[23, 27]. The Fe-rich olivines observed in the CE-5 soil thus likely have derived from the young, highly-evolved basalt in northern Oceanus Procellarum. In contrast, the systematically higher Fo values of olivine in the CE-6 soil (Fig. 4c, d) may be explained by derivation from ejected olivine-bearing, non-mare mafic crustal material (*e.g.*, the anorthosite breccia in the CE-6 soil reported[20]), which is supported by the overall low olivine abundance in the CE-6 basalt clasts[6]. Nearby impact craters, such as the Chaffee S crater, may have delivered these low FeO materials to the CE-6 landing region[8]. The presence of trace amount of highly forsteritic olivine (Fo close to 90) in CE-6 soil possibly reflects minor contribution from the Mg-suite rocks or mantle-derived material[28]. Thus, the wide range of olivine Fo (40 − 90) in CE-6 soil likely reflects diverse lithologies of the non-mare crustal ejecta, underscoring the lithological complexity of the farside lunar crust.

Compositional variation of olivine in lithic fragment and its implications. Compositional zoning of olivine has been intensively investigated and considered as useful proxies of magmatic processes[29, 30]. The partitioning behavior of Fe-Mg between olivine and melt dictates the major element composition of olivine[31] and has received significant attention. Studies have revealed that Fe-Mg partitioning is weakly dependent on temperature, oxygen fugacity, and pressure, but more sensitive to melt composition and water content[32-34]. In zoned olivine, Fe-Mg partitioning is commonly used to trace the crystallization and mixing history of magmas[35]. Traditionally, it has been suggested that gradual changes in the compositions of olivine reflect the progressive variations in the liquid composition from which the olivine crystallized[36]. However, under conditions relevant to mafic-intermediate magmas, the interdiffusion of Fe and Mg occurs rapidly, allowing zoning to develop in initially uniform olivine[37]. Mg could get proportionally more depleted in the olivine than Fe, resulting in compositions that are less forsteritic than under equilibrium conditions. Rapid olivine growth could result in non-equilibrium partitioning, magmas that reduce undercooling through rapid, synchronous crystallization of all their components may contain crystals heavily affected by growth-induced zoning[38].

Considering its mineral assemblage, the olivine-dominated lithic clast in this study is non-basaltic and possibly represent a fragment of lunar crustal rock ejected from neighbouring impact craters. The Mg# range (42.5 to 62.4) is comparable to those of olivine from ferroan anorthosites and alkali-suite, but is significantly lower than those of olivine from the highland Mg-suite[39], and the elevated Al_2O_3 and CaO as well as reduced FeO content compared with CE-5 basalt[6] indicate that it may originated from mafic rocks in the lunar crust. In addition, the high An# of plagioclase (95.1 to 96.0) (Table S7) also supports a FAN affinity (Fig. 5i), consistent with recent observations of close association of olivine and orthopyroxene with plagioclase in CE-6 clasts and their high An# values[20]. The non-concentric, incomplete compositional zoning in the CE-6 olivine (Fig. 5a) appears to be a result of reworking of a previously formed olivine crystal. The irregularity of the zoning may have originated from melting or magma intrusion triggered by impacts[40], resulting in olivine capturing materials from mantle melts or recycled crustal melts, which further supports complex magmatic interactions in the lunar crust-mantle system.

CONCLUSION

This study investigates the particle size and mineralogy of CE-5 and CE-6 lunar soils mainly using Raman spectroscopy. The results highlight significant differences in mineral constitution and particle size distribution of the lunar soil samples, as well as in chemical composition of pyroxene and olivine. Compared to the CE-5 sample, CE-6 soils have slightly larger grain size, slightly higher plagioclase abundance, much higher glass content and lower pyroxene and olivine abundances. In addition, CE-6 pyroxenes have slightly lower MgO and higher FeO contents compared to CE-5 pyroxenes, whereas CE-6 olivines have variable but systematically higher Fo values than CE-5 olivines, with a significant proportion having Fo > 50. These observations are consistent with enhanced impact vitrification and input of more ejected non-mare, diverse crustal material at the CE-6 landing site. Additionally, an olivine crystal in a CE-6 lithic clast exhibits non-concentric, incomplete compositional zoning, indicating complex magmatic interactions in the lunar crust-mantle system that probably involved impact-induced melting and recycling of mantle or crustal material.

Our findings demonstrate the transformative potential of integrating Raman spectroscopy with automated particle characterization systems for achieving non-destructive, multi-parameter analysis of extraterrestrial materials. Future developments in machine learning-driven image recognition, adaptive spectral deconvolution algorithms, and high-throughput data processing architectures promise to refine the spatial and compositional resolution of Raman-based micro-particle analysis. Such advancements will not only optimize analytical workflows for terrestrial laboratory studies of returned samples but also enable in situ mineralogical classification in robotic planetary missions[41].

ASSOCIATED CONTENT

The supporting information (Figs. S1−S2, Tables S1−S8) is available at https://www.at-spectrosc.com.

AUTHOR INFORMATION

Zhenbing She received his BSc in 2001 and PhD in 2007 from the China University of Geosciences (Wuhan). He is a professor of mineralogy and petrology at China University of Geosciences (Wuhan) and the deputy director of the Hubei Key Laboratory of Planetary Geology and Deep-Space Exploration. He has been

developing correlated *in situ* microanalytical techniques integrating micro-Raman spectroscopy, SEM, FIB-TEM, NanoSIMS, ToF-SIMS and synchrotron-based x-ray absorption spectroscopy. His major research interests include the co-evolution of life and environment on the early Earth and studies of potential biosignature on Mars.

Zaicong Wang is a professor at Geochemistry department of China University of Geosciences (Wuhan). He has developed high-precision analytical methods for chalcophile elements and metal stable isotopes to understand the distribution and migration behavior of chalcophile elements within the solid spheres of the Earth in comparison with planetary studies. His interests include chemical composition of Earth's mantle and crust, early accretion and evolution of Earth and Moon, the transportation of metal and volatile elements in subduction zones, secular crust-mantle interaction and its impacts on giant gold mineralization in eastern North China Craton. He has published 52 papers as first or corresponding author in leading journals such as Nature, Nature Geoscience, Nature Astronomy, Nature Communications, Geology, PNAS, EPSL, and GCA. He serves as the Associate Editor of GCA and Editorial Board Member of EPSL, and has received the Excellent Young Scientist Grant of NSFC, the GaoShan and Houdefeng Young Scientist Awards, and Hubei Youth May Fourth Medal.

ACKNOWLEDGMENTS

This work was supported by the National Natural Science Foundation of China (42441802, 42241156), Scientific Research Innovation Capability Support Project for Young Faculty (ZYGXQNJSKYCXNLZCXM-P6), and the Outstanding Youth Team project of China University of Geosciences, Wuhan (G1323523042). We are grateful to all staff of the Chang'e-6 mission for their efforts that make this work possible. The sample used in this study was provided by the China National Space Administration.

REFERENCES

1. S. Hu, H. C. He, J. L. Ji, Y. T. Lin, H. J. Hui, M. Anand, R. Tartèse, Y. H. Yan, J. L. Hao, R. Y. Li, L. X. Gu, Q. Guo, H. Y. He, and Z. Y. Ouyang, *Nature*, 2021, **600**, 49-53. https://doi.org/10.1038/s41586-021-04107-9
2. H.-C. Tian, H. Wang, Y. Chen, W. Yang, Q. Zhou, C. Zhang, H.-L. Lin, C. Huang, S.-T. Wu, L.-H. Jia, L. Xu, D. Zhang, X.-G. Li, R. Chang, Y.-H. Yang, L.-W. Xie, D.-P. Zhang, G.-L. Zhang, S.-H. Yang, and F.-Y. Wu, *Nature*, 2021, **600**, 59-63. https://doi.org/10.1038/s41586-021-04119-5
3. C. L. Li, H. Hu, M.-F. Yang, Z.-Y. Pei, Q. Zhou, X. Ren, B. Liu, D. W. Liu, X. G. Zeng, G. L. Zhang, H. B. Zhang, J. J. Liu, Q. Wang, X. J. Deng, C. J. Xiao, Y. G. Yao, D. S. Xue, W. Zuo, Y.Su, W.B. Wen, and Z. Y. Ouyang, *Natl. Sci. Rev.*, 2022, **9**, nwab188. https://doi.org/10.1093/nsr/nwab188
4. B.-W. Wang, Q. W. L. Zhang, Y. Chen, W. H. Zhao, Y. Liu, G.-Q. Tang, H.-X. Ma, B. Su, H. J. Hui, J. W. Delano, F.-Y Wu, X.-H. Li, Y. Y. He, and Q.-L. Li, *Science*, 2024, **385**, 1077-1080. https://doi.org/10.1126/science.adk6635
5. X. G. Zeng, D. W. Liu, Y. Chen, Q. Zhou, X. Ren, Z. B. Zhang, W. Yan, W. L. Chen, Q. Wang, X. J. Deng, H. Hu, J. J. Liu, W. Zou, J. W. Head, and C. L. Li, *Nat. Astron.*, 2023, **7**, 1188-1197. https://doi.org/10.1038/s41550-023-02038-1
6. C. L. Li, H. Hu, M.-F. Yang, J. J. Liu, Q. Zhou, X. Ren, B. Liu, D. W. Liu, X. G. Zeng, W. Zuo, G. L. Zhang, H. B. Zhang, S. H. Yang, Q. Wang, X.J. Deng, X. Y. Gao, Y.Su, W. B. Wen, and Z. Y. Ouyang, *Natl. Sci. Rev.*, 2024, **11**, nwae328. https://doi.org/10.1093/nsr/nwae328
7. Y. Q. Qian, J. Head, J. Michalski, X. Wang, C. H. van der Bogert, H. Hiesinger, L. Z. Sun, W. Yang, L. Xiao, X. H. Li, and G. C. Zhao, *Earth Planet. Sci. Lett.*, 2024, **637**, 118737. https://doi.org/10.1016/j.epsl.2024.118737
8. Z. Y. Yue, S. Gou, S. J. Sun, W. Yang, Y. Chen, Y. X. Wang, H. L. Lin, K. C. Di, Y. T. Lin, X. H. Li, and F. Y. Wu, *The Innovation*, 2024, **5**, 100663. https://doi.org/10.1016/j.xinn.2024.100663
9. J.-H. Li, Q.-L. Li, L. Zhao, J.-H. Zhang, X. Tang, L.-X. Gu, Q. Guo, H.-X. Ma, Q. Zhou, Y. Liu, P.-Y. Liu, H. Qiu, G. Li, L. Gu, S. Guo, C.-L. Li, X.-H. Li, F.-Y. Wu, and Y.-X. Pan, *Geosci. Front.*, 2022, **13**, 101367. https://doi.org/10.1016/j.gsf.2022.101367
10. K. N. Cao, M. T. Dong, Z. B. She, Q. Xiao, X. Y. Wang, Y. Q. Qian, Y. H. Li, Z. C. Wang, Q. He, X. Wu, K. Q. Zong, Z. C. Hu, and L. Xiao, *Sci. China Earth Sci.*, 2022, **65**, 1704-1714. https://doi.org/10.1007/s11430-022-9966-5
11. P. McMillan, *Am. Mineral.*, 1984, **69**, 622-644. https://pubs.geoscienceworld.org/msa/ammin/article-pdf/69/7-8/622/4217030/am69_622.pdf
12. A. Wang, B. L. Jolliff, and L. A. Haskin, *J. Geophys. Res.-Planet.*, 1995, **100**, 21189-21199. https://doi.org/10.1029/95JE02133
13. S. K. Sharma, P. G. Lucey, M. Ghosh, H. W. Hubble, and K. A. Horton, *Spectrochim. Acta A*, 2003, **59**, 2391-2407. https://doi.org/10.1016/S1386-1425(03)00080-5
14. B. Wopenka, *Earth Planet. Sci. Lett.*, 1988, **88**, 221-231. https://doi.org/10.1016/0012-821X(88)90079-9
15. W. Zhang, Q. Liang, X. J. Li, L.-P. Ma, X. Y. Li, Z. Z. Zhao, R. Zhang, H. T. Cao, Z. Z. Wang, W. W. Li, Y. N. Wang, M. Q. Liu, N. L. Yue, H. Y. Liu, Z. Y. Hu, L. Liu, Q. Zhou, F. F. Li, W. T. Zheng, W. C. Ren, and M. Zou, *Natl. Sci. Rev.*, 2024, **11**, nwae211. https://doi.org/10.1093/nsr/nwae211
16. L. A. Haskin, A. Wang, K. M. Rockow, B. L. Jolliff, R. L. Korotev, and K. M. Viskupic, *J. Geophys. Res.-Planet.*, 1997, **102**, 19293-19306. https://doi.org/10.1029/97JE01694
17. Q. He, Y. H. Li, I. Baziotis, Y. Q. Qian, L. Xiao, Z. C. Wang, W. Zhang, B. J. Luo, C. R. Neal, J. M. D. Day, F. Pan, Z. B. She, X. Wu, Z. C. Hu,K. Q. Zong, and L. Wang, *Icarus*, 2022, **383**, 115082. https://doi.org/10.1016/j.icarus.2022.115082
18. A. Wang, B. L. Jolliff, L. A. Haskin, K. E. Kuebler, and K. M. Viskupic, *Am. Mineral.*, 2001, **86**, 790-806. https://doi.org/10.2138/am-2001-0703

19. L. Borromeo, S. Andò, D. Bersani, E. Garzanti, P. Gentile, L. Mantovani, and M. Tribaudino, *Chem. Geol.*, 2023, **635**, 121610. https://doi.org/10.1016/j.chemgeo.2023.121610

20. Z. C. Wang, Y. H. Li, J. W. Li, K. Q. Zong, Z. B. She, Q. He, J. W. Zhao, W. Zhang, J. Q. Zheng, F. B. Pan, T.Luo, K. Crnobrnja, X. Chen, L. Xiao, Z. C. Hu, X. Wu, Y. S. Liu, and F. Moynier, *Geology*, 2025, **53**, 557-561. https://doi.org/10.1130/G53086.1

21. Q. W. L. Zhang, M.-H. Yang, Q.-L. Li, Y. Liu, Z.-Y. Yue, Q. Zhou, L.-Y. Chen, H.-X. Ma, S.-H. Yang, X. Tang, G.-L. Zhang, X. Ren and X.-H. Li, *Nature*, 2025, **643**, 356-360. https://doi.org/10.1038/s41586-024-08382-0

22. Z. X. Cui, Q. Yang, Y.-Q. Zhang, C. Y. Wang, H. Y. Xian, Z. M. Chen, Z. Y. Xiao, Y. Qian, J. W. Head III, C. R. Neal, L. Xiao, F. L. Luo, J. Y. Chen, P. L. He, Y. H. Cao, Q. Zhou, F. F. Huang, L. L. Chen, B. Wei, J. T. Wang, Y.-N. Yang, S. Li, Y. P. Yang, X. J. Lin, J. X. Zhu, L. Zhang and Y.-G. Xu, *Science*, 2024, **386**, 1395-1399. https://doi.org/10.1126/science.adt1093

23. Z. C. Wang, K. Q. Zong, Y. H. Li, J. W. Li, Q. He, Z. Q. Zou, H. Becker, F. Moynier, J. M. D. Day, W. Zhang, Y. Q. Qian, L. Xiao, Z. C. Hu, Z. B. She, H. J. Hui, X. Xu, and Y. S. Liu, *Geochim. Cosmochim. Ac.*, 2024, **373**, 17-34. https://doi.org/10.1016/j.gca.2024.03.029

24. G. J. Taylor, L. M. Martel, P. G. Lucey, J. J. Gillis-Davis, D. F. Blake, and P. Sarrazin, *Geochim. Cosmochim. Ac.*, 2019, **266**, 17-28. https://doi.org/10.1016/j.gca.2019.07.046

25. H. J. Cao, J. Chen, X. J. Lu, J. Q. Kong, L. Qiao, C. X. Yin, C. Q. Liu, H. K. Qu, X. H. Fu, Y. Q. Xin and Z. C. Ling, *Commun. Earth Environ.*, 2025, **6**, 522. https://doi.org/10.1038/s43247-025-02441-8

26. O. S. Barnouin, R. T. Daly, M. J. Cintala, and D. A. Crawford, *Icarus*, 2019, **325**, 67-83. https://doi.org/10.1016/j.icarus.2019.02.004

27. K. Q. Zong, Z. C. Wang, J. W. Li, Q. He, Y. H. Li, H. Becker, W. Zhang, Z. C. Hu, T. He, K. N. Cao, Z. B. She, X. Wu, L. Xiao, and Y. S. Liu, *Geochim. Cosmochim. Ac.*, 2022, **335**, 284-296. https://doi.org/10.1016/j.gca.2022.06.037

28. S.-Z. Sheng, S.-J. Wang, Q.-L. Li, S. T. Wu, H. Wang, J.-X. Hua, Z. Y. Chen, J.-H. Hao, B. Zhang, Y. S. He and J.-M. Zhu, *Nat. Commun.*, 2025, **16**, 3759. https://doi.org/10.1038/s41467-025-58820-4

29. B. Gordeychik, T. Churikova, A. Kronz, C. Sundermeyer, A. Simakin, and G. Wörner, *Sci. Rep.*, 2018, **8**, 11775. https://doi.org/10.1038/s41598-018-30133-1

30. M. J. Pankhurst, D. J. Morgan, T. Thordarson, and S. C. Loughlin, *Earth Planet. Sci. Lett.*, 2018, **493**, 231-241. https://doi.org/10.1016/j.epsl.2018.04.025

31. N. L. Bowen and J. F. Schairer, *Am. J. Sci.*, 1935, **s5-29**, 151-217. https://doi.org/10.2475/ajs.s5-29.170.151

32. J. Longhi, D. Walker, and J. F. Hays, *Geochim. Cosmochim. Ac.*, 1978, **42**, 1545-1558. https://doi.org/10.1016/0016-7037(78)90025-X

33. A. K. Matzen, M. B. Baker, J. R. Beckett, and E. M. Stolper, *J. Petrol.*, 2011, **52**, 1243-1263. https://doi.org/10.1093/petrology/egq089

34. J. Blundy, E. Melekhova, L. Ziberna, M. C. S. Humphreys, V. Cerantola, R. A. Brooker, C. A. McCammon, M. Pichavant, and P. Ulmer, *Contrib. Mineral. Petr.*, 2020, 175, 103. https://doi.org/10.1007/s00410-020-01736-7

35. F. Costa and M. Dungan, *Geology*, 2005, **33**, 837-840. https://doi.org/10.1130/G21675.1

36. S. Chakraborty, *Rev. Mineral. Geochem.*, 2010, **72**, 603-639. https://doi.org/10.2138/rmg.2010.72.13

37. F. Costa, T. Shea, and T. Ubide, *Nat. Rev. Earth Environ.*, 2020, **1**, 201-214. https://doi.org/10.1038/s43017-020-0038-x

38. T. Shea, A. K. Matzen, and A. J. Mourey, *Contrib. Mineral. Petrol.*, 2022, **177**, 114. https://doi.org/10.1007/s00410-022-01969-8

39. C. K. Shearer, D. P. Moriarty, S. B. Simon, N. Petro, and J. J. Papike, *J. Geophys. Res.-Planet.*, 2023, **128**, e2022JE007409. https://doi.org/10.1029/2022JE007409

40. D. P. Moriarty III, R. N. Watkins, S. N. Valencia, J. D. Kendall, A. J. Evans, N. Dygert, and N. E. Petro, *J. Geophys. Res.-Planet.*, 2021, **126**, e2020JE006589. https://doi.org/10.1029/2020JE006589

41. H. T. Zhao, X. F. Liu, W. M. Xu, D. Y. T. Wen, J. N. Xie, Z. Q. Zhang, Z. Q. Jiang, Z. C. Ling, Z. P. He, R. Shu, and H. Y. Wang, *Remote Sens.*, 2025, **17**, 860. https://doi.org/10.3390/rs17050860

42. K. E. Kuebler, B. L. Jolliff, A. Wang, and L. A. Haskin, *Geochim. Cosmochim. Ac.*, 2006, **70**, 6201-6222. https://doi.org/10.1016/j.gca.2006.07.035